Numerical modeling of avalanches based on Saint Venant equations using a kinetic scheme

A. Mangeney-Castelnau,[1] J.-P. Vilotte,[1] M. O. Bristeau,[2] B. Perthame,[3] F. Bouchut,[3] C. Simeoni,[3] and S. Yerneni[4]

Received 13 June 2002; revised 13 February 2003; accepted 27 June 2003; published 15 November 2003.

[1] Numerical modeling of debris avalanche is presented here. The model uses the long-wave approximation based on the small aspect ratio of debris avalanches as in classical Saint Venant model of shallow water. Depth-averaged equations using this approximation are derived in a reference frame linked to the topography. Debris avalanche is treated here as a single-phase, dry granular flow with Coulomb-type behavior. The numerical finite volume method uses a kinetic scheme based on the description of the microscopic behavior of the system to define numerical fluxes at the interfaces of a finite element mesh. The main advantage of this method is to preserve the height positivity. The originality of the presented scheme stands in the introduction of a Dirac distribution of particles at the microscopic scale in order to describe the stopping of a granular mass when the driving forces are under the Coulomb threshold. Comparisons with analytical solutions for dam break problems and experimental results show the efficiency of the model in dealing with significant discontinuities and reproducing the flowing and stopping phase of granular avalanches. The ability of the model to describe debris avalanche behavior is illustrated here by schematic numerical simulation of an avalanche over simplified topography. Coulomb-type behavior with constant and variable friction angle is compared in the framework of this simple example. Numerical tests show that such an approach not only provides insights into the flowing and stopping stage of the granular mass but allows observation of interesting behavior such as the existence of a fluid-like zone behind a stopped solid-like granular mass in specific situations, suggesting the presence of horizontal surfaces in the deposited mass. *INDEX TERMS:* 3210 Mathematical Geophysics: Modeling; 3230 Mathematical Geophysics: Numerical solutions; 5415 Planetology: Solid Surface Planets: Erosion and weathering; 8499 Volcanology: General or miscellaneous; 9810 General or Miscellaneous: New fields (not classifiable under other headings); *KEYWORDS:* avalanche modeling, Coulomb friction, Saint Venant equations, finite volume kinetic scheme, gravitational flow

Citation: Mangeney-Castelnau, A., J.-P. Vilotte, M. O. Bristeau, B. Perthame, F. Bouchut, C. Simeoni, and S. Yerneni, Numerical modeling of avalanches based on Saint Venant equations using a kinetic scheme, *J. Geophys. Res.*, *108*(B11), 2527, doi:10.1029/2002JB002024, 2003.

1. Introduction

[2] Granular avalanches such as rock or debris flows regularly cause large amounts of human and material damages. Numerical simulation of granular avalanches should provide a useful tool for investigating, within realistic geological contexts, the dynamics of these flows and of their arrest phase and for improving the risk assessment of such natural hazards. Risk evaluation of these events requires the comprehension of two fundamental problems: the initiation and the destabilization phase and in the other hand the flowing and stopping phase. Even though the specification of the initial conditions is a primary problem which is not yet resolved, we concentrate here on the description of the flowing and stopping phase. It is worth to mention that by construction the flow models generally do not address the problem of the initiation and the destabilization phase of an avalanche.

[3] During a granular avalanche, the characteristic length in the flowing direction is generally much larger than the vertical one, e.g., the avalanche thickness. Such a long-wave scaling argument has been widely used in the derivation of continuum flow models for granular avalanches [e.g., *Hunt*, 1985; *Iverson*, 1997, *Iverson and Denlinger*, 2001; *Jenkins and Askari*, 1999; *Savage and Hutter*, 1989; *Hutter et al.*, 1995; *Douady et al.*, 1999]. This leads to depth-averaged

[1]Département de Modélisation Physique et Numérique, Institut de Physique du Globe de Paris, Paris, France.
[2]Institut National de Recherche en Informatique et en Automatique, Le Chesnay, France.
[3]Département de Mathématique et Applications, Ecole Normale Supérieure et CNRS, Paris, France.
[4]Center for Development of Advanced Computing, Pune University Campus, Pune, India.

0148-0227/03/2002JB002024$09.00

models governed by generalized Saint Venant equations. These models provide a fruitful paradigm for investigating the dynamics and the extent of granular avalanches in the presence of smooth topography [*Hutter et al.*, 1995; *Naaim et al.*, 1997; *Pouliquen*, 1999]. Granular surface flow models are closely related to other Saint Venant models used in ocean and hydraulic engineering to describe both wave propagation, hydraulic jump and open channel flow among others.

[4] The physics and the rheology of granular avalanches are indeed challenging problems and the subject of an active research [e.g., *Hunt*, 1994; *Laigle and Coussot*, 1997; *Arattano and Savage*, 1994; *Macedonio and Pareschi*, 1992; *Whipple*, 1997; *Iverson*, 1997]. Despite the lack of a clear physical understanding of avalanche flow, useful basic behavior of granular avalanches can be derived from experimental approaches [e.g., *Pouliquen*, 1999; *Douady et al.*, 1999]. Without going into detailed rheological assumptions, which would be rather uncertain due to the lack of a physical understanding of the actual forces acting in debris avalanches, it is of interest here to emphasize some of the characteristics that make such flows quite specific. The first characteristic is that granular media has the ability to remain static (solid) even along an inclined surface. This observation is related since Coulomb to some macroscopic solid-like friction and the system is able to flow only when the driving force reaches a critical value. In classical Coulomb's friction, the friction coefficient remains constant [e.g., *Hutter et al.*, 1995; *Naaim et al.*, 1997]. More evolved friction models, which assume a friction coefficient that depends on both the avalanche mean velocity and thickness, has been recently proposed [*Pouliquen*, 1999; *Douady et al.*, 1999] on the basis of laboratory experiments and theoretical assumptions. These models have been shown quite useful to explain the geometry of the granular flow as well as the observed runout of granular avalanches. In both cases, the existence of a macroscopic friction threshold leads to non smooth dynamics that has to be handled within appropriate mathematical and numerical formulations. The second characteristic is that topography along which the avalanche is flowing can be quite steep and rough. Long-wave approximation has therefore to be derived in a reference frame locally tangent to the bedrock or to the free surface of the flow, in contrast to the gravity frame of reference used in classical Saint Venant models in hydraulic engineering. The definition of such a tangent frame of reference is not obvious for a realistic earth topography and is still a challenging problem.

[5] Computational methods developed in geophysics for solving the governing conservation laws of debris avalanches have mostly focused on the resolution of shock waves and surges. They are based on fractional step methods and high resolution approximate Riemann solvers like the Harten-Lax-van Leer (HLL) solver [*Toro*, 1997]. Most of these methods are based on conservative non-oscillatory finite differences [*Gray et al.*, 1999; *Wieland et al.*, 1999; *Tai*, 2000; *Tai et al.*, 2002] or finite volumes which do have the nice property of being conservative with respect to the flow height [*Naaim et al.*, 1997; *Laigle and Coussot*, 1997; *Denlinger and Iverson*, 2001]. They are based on an Eulerian formulation, a Lagrangian formulation [*Zwinger*, 2000] or a Lagrangian-Eulerian operator splitting [*Mangeney et al.*, 2000]. These Riemann methods do present significant improvements over the early Lagrangian finite difference methods [*Savage and Hutter*, 1989, 1991; *Greve et al.*, 1994]. However, they do not preserve height positivity, and specific numerical development has to be introduced in the wetting-drying transition where the system loses hyperbolicity or an artificial small height is introduced in the regions where no fluid is present as in the work by *Heinrich et al.* [2001].

[6] We consider here an alternative numerical scheme to compute debris avalanches based on the kinetic interpretation of the system which intrinsically preserves height positivity. Kinetic schemes have been proposed by *Audusse et al.* [2000] and *Bristeau et al.* [2001] to compute Saint Venant equation in hydraulic problems. A survey of the theoretical properties of these schemes is given by *Perthame* [2002]. Recently, kinetic schemes have been extended to include stiff source term [*Botchorishvilli et al.*, 2000; *Perthame and Simeoni*, 2001]. Kinetic schemes have been shown to preserve the height positivity and to be able to treat the wetting-drying transition. However, classical kinetic schemes do not allow solid/fluid-like transitions, associated with a nonsmooth friction. The idea of the present scheme is to introduce a "zero temperature" kinetic approximation when the driving force is under the Coulomb threshold (solid-like behavior).

[7] We first present here the basic equations and conservation laws which govern the evolution of granular avalanches along a realistic topography. In particular, using classical scaling arguments for surface flow, we derive the depth averaged Saint Venant equations in a reference frame linked to the bed topography and we review some minimal assumptions, inspired from experiments, on the characteristics of the frictional behavior of granular avalanches. Then we present a numerical scheme based on a finite volume approximation of the governing set of conservation laws. At this stage, we introduce a kinetic solver which takes into account the existence of a friction threshold. The accuracy of this kinetic scheme is assessed against the classical dam break problem over an inclined plane and the validation of the flowing and the stopping phase is performed by comparing the numerical results with laboratory experiments. Finally a simple application of the model is performed by simulating a debris avalanche over a schematic bed topography. Comparisons between models with constant and nonconstant friction are discussed based on the runout distance, the shape of the deposit and the mechanism of the stopping phase.

2. Equations

[8] Debris avalanches are described here within a continuum theoretical framework as a single-phase, incompressible material with constant density [e.g., *Savage and Hutter*, 1989; *Iverson and Denlinger*, 2001]. The evolution is therefore governed at time $t \geq 0$ by the mass and momentum conservation laws:

$$\nabla \cdot \mathbf{u} = 0, \tag{1}$$

$$\rho\left(\frac{\partial \mathbf{u}}{\partial t} + \mathbf{u}\cdot\nabla\mathbf{u}\right) = -\nabla\cdot\sigma + \rho\mathbf{g}, \tag{2}$$

where $\mathbf{u}(x, y, z, t) = (u(x, y, z, t), v(x, y, z, t), w(x, y, z, t))$ denotes the three-dimensional velocity vector inside the avalanche in a (x, y, z) coordinate system that will be discussed later, $\boldsymbol{\sigma}(x, y, z, t)$ is the Cauchy stress tensor, ρ the mass density, and $\mathbf{g}$ the gravitational acceleration. The bottom boundary, or bed, is described by a surface $\psi_b(x, y, z, t) = z - b(x, y) = 0$ and the free surface of the flow by $\psi_s(x, y, z, t) = z - s(x, y, t) \equiv z - b(x, y) - h(x, y, t) = 0$, where where $h(x, y, t)$ is the depth of the avalanche layer and $s(x, y, t)$ is the free surface elevation.

[9] A kinematic boundary condition is imposed on the free and the bed surfaces, that specifies that mass neither enters nor leaves at the free surface or at the base:

$$\frac{\mathrm{d}\psi_s}{\mathrm{d}t}|_s = \left(\frac{\partial \psi_s}{\partial t} + \mathbf{u}\cdot\nabla\psi_s\right)|_s = 0, \tag{3}$$

$$\frac{\mathrm{d}\psi_b}{\mathrm{d}t}|_b = \left(\frac{\partial \psi_b}{\partial t} + \mathbf{u}\cdot\nabla\psi_b\right)|_b = 0, \tag{4}$$

as well as a stress free boundary condition at the surface, neglecting the atmospheric pressure

$$\boldsymbol{\sigma}\cdot\mathbf{n}_s = 0, \tag{5}$$

where $\mathbf{n_s}$ denotes the unit vector normal to the free surface.

[10] Depth averaging of these equations and shallow flow assumption require the choice of an appropriate coordinate system. During the flow, the avalanche thickness is much smaller than its extent parallel to the bed. In the case of significant slopes, the shallow flow assumption is more significant in a reference frame linked to the topography and the classical shallow water approximation relating horizontal and vertical direction is not appropriate. As in the work by *Denlinger and Iverson* [2001], the equations are written here in terms of a local, orthogonal Cartesian coordinate system in which the z coordinate is normal to the local topography. We define a local x axis corresponding to the projection of an arbitrary fixed $\tilde{x}$ direction in the local tangent plane to the topography and $\mathbf{y} = \mathbf{z} \wedge \mathbf{x}$ (Figure 1). Note that the choice of an appropriate reference frame is not straightforward and may lead to a nonorthonormal coordinate system as by *Heinrich et al.* [2001], *Assier-Rzadkiewicz et al.* [2000] or *Sabot et al.* [1998]. The variation in space of a local coordinate system introduces errors in the calculation of the derivatives requiring slow variation of the bedrock. The equations developed in a coordinate system linked to the topography are not directly applicable in a fixed reference frame as was performed by *Naaim et al.* [1997] and *Naaim and Gurer* [1998]: appropriate rotation has to be used to transform properly topography-linked equations in a fixed reference frame [see, e.g., *Douady et al.*, 1999].

[11] In the reference frame linked to the topography, equations of mass and momentum in the x and y direction derived by the integration of Navier-Stokes equations (1), and (2) with boundary conditions (3)–(5) read

$$\frac{\partial h}{\partial t} + \mathrm{div}(h\bar{\mathbf{u}}) = 0, \tag{6}$$

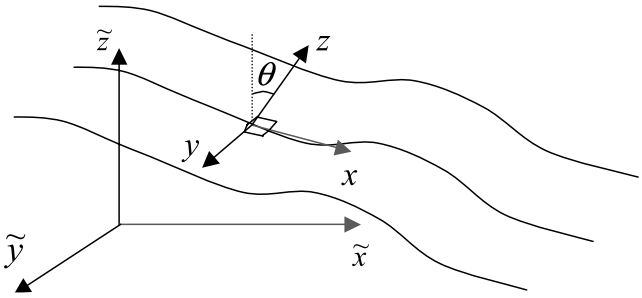

Figure 1. Reference frame (x, y, z) linked to the topography and galilean reference frame $(\tilde{x}, \tilde{y}, \tilde{z})$ with θ the steepest slope angle.

$$\frac{\partial}{\partial t}(h\bar{u}) + \frac{\partial}{\partial x}\left(h\overline{u^2}\right) + \frac{\partial}{\partial y}(h\overline{uv}) = \gamma_x gh + \frac{1}{\rho}\frac{\partial}{\partial x}(h\overline{\sigma}_{xx}) + \frac{1}{\rho}\frac{\partial}{\partial y}\left(h\overline{\sigma}_{xy}\right) + \frac{1}{\rho}T_x, \tag{7}$$

$$\frac{\partial}{\partial t}(h\bar{v}) + \frac{\partial}{\partial x}(h\overline{uv}) + \frac{\partial}{\partial y}\left(h\overline{v^2}\right) = \gamma_y gh + \frac{1}{\rho}\frac{\partial}{\partial x}\left(h\overline{\sigma}_{xy}\right) + \frac{1}{\rho}\frac{\partial}{\partial y}\left(h\overline{\sigma}_{yy}\right) + \frac{1}{\rho}T_y, \tag{8}$$

where $\bar{\mathbf{u}} = (\bar{u}, \bar{v})$ denotes the depth-averaged flow velocity in the reference frame (x, y, z) defined below, h the fluid depth, and γ_i are coefficients, function of the local slope, defining the projection of the gravity vector along the i direction. The traction vector $\mathbf{T} = (T_x, T_y, T_z) = -\boldsymbol{\sigma} \cdot \mathbf{n_b}$, where $\mathbf{n}_b$ is the unit vector normal to the bed, read

$$\mathbf{T} = \begin{pmatrix} \sigma_{xx}\frac{\partial b}{\partial x} + \sigma_{xy}\frac{\partial b}{\partial y} - \sigma_{xz} \\ \sigma_{xy}\frac{\partial b}{\partial x} + \sigma_{yy}\frac{\partial b}{\partial y} - \sigma_{yz} \\ \sigma_{xz}\frac{\partial b}{\partial x} + \sigma_{yz}\frac{\partial b}{\partial y} - \sigma_{zz} \end{pmatrix}_b, \tag{9}$$

where the notation f_b indicates the value of f at the base (at $z = 0$). Note that equations (6)–(8) are obtained without any approximation. In the following, we will underline the assumptions (long-wave approximation and the specification of a friction law) leading to simplify and close the equations.

2.1. Approximation

[12] A small aspect ratio $\epsilon = H/L$, where H and L are two characteristic dimensions along the z axis and in the plane xOy, respectively is then introduced in the depth-averaged x and y equations (equations (7) and (8)) and in the nondepth-averaged z equation obtained from the z projection of equation (2). An asymptotic analysis with respect to ϵ [e.g., *Gray et al.*, 1999] leads to neglect the acceleration normal to the topography and the horizontal gradients of the stresses in the z equation, leading to

$$\sigma_{zz} = \rho g \gamma_z (h - z), \tag{10}$$

where $\gamma_z = \cos\theta$, with θ defined as the angle between the vertical axis and the normal to the topography (Figure 1). Note that neglecting the horizontal gradients $\partial\, \sigma_{iz}/\partial\, x_i$ for

$i = x, y$ in the z equation do not allows to neglect $\sigma_{iz|b}$ (at the base) in T_x and T_y [*Gray et al.*, 1999]. From the scale analysis with respect to ϵ, the normal traction reduced to $T_z = -\sigma_{zz|b}$ and $(\partial/\partial x_i)$ $(h\overline{\sigma}_{xy})$ can be neglected in the x and y depth-averaged momentum equations.

[13] The shape of the vertical profile of the horizontal velocity in debris avalanche flow is still an open question. The conservation of the initial stratigraphy sometimes observed in the deposits of a debris avalanche has led to the assumption that all the deformation is essentially located in a fine boundary layer near the bed surface, so that the horizontal velocity is approximately constant over the depth [e.g., *Savage and Hutter*, 1989; *Naaim et al.*, 1997]. More recently, laboratory experiments on granular flows suggest a linear profile of the horizontal velocity [*Azanza*, 1998; *Douady et al.*, 1999]. A weak influence of the vertical profile of the horizontal velocity has been observed by *Pouliquen and Forterre* [2002] for granular flows over inclined plane. Note that in the locally tangent frame of reference, simple assumption for the velocity profile (e.g., constant or linear profile) can be made unlike in the galilean fixed reference frame. We assume here a vertically constant velocity so that $\overline{u_i u_j} = \overline{u}_i \overline{u}_j$. In the following, the overline will be dropped and (u, v) will represent the mean velocity field.

2.2. Flow and Friction Law

[14] We consider here the minimal model by assuming isotropy of normal stresses, i. e. $\sigma_{xx} = \sigma_{yy} = \sigma_{zz}$ contrary to *Savage and Hutter* [1989] where earth pressure coefficients are defined as the ratio of the longitudinal stresses to the normal stress. A relation deduced from the mechanical behavior of the material has to be imposed between the tangential stress $\mathbf{T}_t = (T_x, T_y)$, and $\mathbf{u}$ and h in order to close equations (6), (7), (8). The depth-averaged mass is then considered as an effective material submitted to an empirical friction introduced in the tangential traction term $\mathbf{T}_t$ in a way similar to the experimental approach of *Pouliquen* [1999].

[15] Dissipation in granular materials is generally described by a Coulomb-type friction law relating the norm of the tangential traction $\|\mathbf{T}_t\|$ at the bed to the norm of the normal traction $\|\mathbf{T}_n\| = |T_z| = |\sigma_{zz|b}|$ at the bed, through a factor $\mu = \tan\delta$ involving the dynamic friction angle δ

$$\| \mathbf{T}_t \| \leq \sigma_c = \mu \| \mathbf{T}_n \| = \mu |\sigma_{zz|b}|, \tag{11}$$

and acting opposite to the velocity. The value of σ_c defines the upper bound of the admissible stresses. In the considered coordinate system, using equation (10), σ_c read

$$\sigma_c = \mu \rho g \gamma_z h. \tag{12}$$

The resulting Coulomb-type behavior can be summarized

$$\| \mathbf{T}_t \| \geq \sigma_c \Rightarrow T_i = -\sigma_c \frac{u_i}{\| \mathbf{u} \|}, \tag{13}$$

$$\| \mathbf{T}_t \| < \sigma_c \Rightarrow \mathbf{u} = 0, \tag{14}$$

where $i = x, y$. The application of this behavior poses the problem of the evaluation of $\mathbf{T}_t$ as will be described in section 3.3.

[16] Laboratory experiments [*Pouliquen*, 1999] have shown that laws involving constant friction angle are restricted to granular flows over smooth inclined planes or to flows over rough bed with high inclination angles. The assumption of constant friction angle seems to fail for granular flows over rough bedrock for a range of inclination angles, for which steady uniform flows can be observed [*Pouliquen*, 1999]. In this range, the frictional force is able to balance the gravity force indicating a shear rate dependence. *Pouliquen* [1999] proposed an empirical friction coefficient $\mu = \tan\delta$ as a function of the Froude number $\|\mathbf{u}\|/\sqrt{gh}$ and the thickness h of the granular layer

$$\mu(\| \mathbf{u} \|, h) = \tan\delta_1 + (\tan\delta_2 - \tan\delta_1) \exp\left(-\beta \frac{h}{d} \frac{\sqrt{gh}}{\| \mathbf{u} \|}\right), \tag{15}$$

where δ_1, δ_2, and d are characteristics of the material which can be measured from the deposit properties. d is a length characterizing the friction law, which is scaled on the mean diameter of particles. In the case of spherical glass particles used in these laboratory experiments d is of the order of the diameter of the beads and $\beta = 0.136$ [*Pouliquen*, 1999]. Equation (15) provides a friction angle, ranging between two values δ_1 and δ_2, depending on the values of the velocity and thickness of the flow. The friction coefficient μ is higher for small values of the thickness and high values of the velocity contrary to the proposed function of *Gray et al.* [1999] where lowest elevations (e.g., the rear and the front) are subject to small friction. What this empirical law means in terms of microscopic forces is still an open problem. Hydraulic model using this flow law has been shown to be able to predict the spreading of a granular mass from release to deposit [*Pouliquen and Forterre*, 2002].

2.3. Governing Equations

[17] Finally, the depth-averaged stress tensor and the traction vector involved in the x and y depth-averaged equations reduce to

$$\overline{\boldsymbol{\sigma}} = \begin{pmatrix} \rho g \gamma_z \frac{h}{2} & 0 & 0 \\ 0 & \rho g \gamma_z \frac{h}{2} & 0 \\ 0 & 0 & \rho g \gamma_z \frac{h}{2} \end{pmatrix}, \tag{16}$$

and if $\|\mathbf{T}_t\| \geq \sigma_c$

$$\mathbf{T} = \begin{pmatrix} -\mu \rho g \gamma_z h \frac{u_x}{\|\mathbf{u}\|} \\ -\mu \rho g \gamma_z h \frac{u_y}{\|\mathbf{u}\|} \\ -\rho g \gamma_z h \end{pmatrix}, \tag{17}$$

respectively, and the resulting set of equations reads

$$\frac{\partial h}{\partial t} + \mathrm{div}(h\mathbf{u}) = 0, \tag{18}$$

and if $\|T_t\| \geq \sigma_c$, the granular mass is flowing following the dynamical equations

$$\frac{\partial}{\partial t}(hu) + \frac{\partial}{\partial x}(hu^2) + \frac{\partial}{\partial y}(huv) = \gamma_x gh + \frac{\partial}{\partial x}\left(g\gamma_z \frac{h^2}{2}\right) - \mu g \gamma_z h \frac{u_x}{\| \mathbf{u} \|}, \tag{19}$$

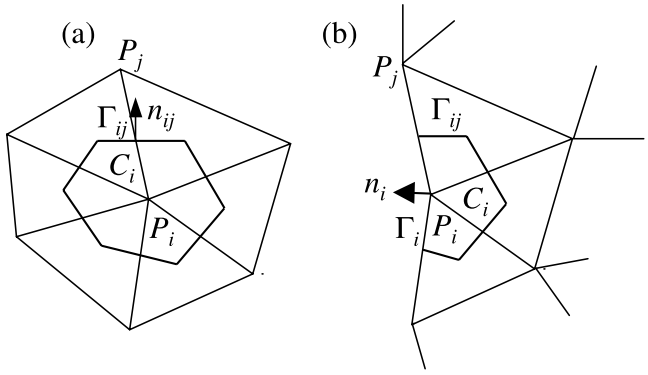

Figure 2. Triangular finite element mesh for (a) dual inner cell C_i and (b) dual boundary cell C_i.

$$\frac{\partial}{\partial t}(hv)+\frac{\partial}{\partial x}(huv)+\frac{\partial}{\partial y}(hv^2)=\gamma_y gh+\frac{\partial}{\partial y}\left(g\gamma_z\frac{h^2}{2}\right)-\mu g\gamma_z h\frac{u_y}{\|\mathbf{u}\|}, \tag{20}$$

or if $\|T_t\| < \sigma_c$, the granular mass stops and the momentum equations are replaced by $\mathbf{u} = 0$. The evaluation of $\mathbf{T}_t$ is achieved by using a classical resolution method for nonsmooth mechanics [see, e.g., *Staron*, 2002] and will be developed in section 3.3.

3. Numerical Model

3.1. Finite Volume Method

[18] The model developed here is based on the classical finite volume approach for solving hyperbolic systems using the concept of cell centered conservative quantities. This type of methods requires the formulation of the equation in terms of conservation laws. The system of equations (18), (19), and (20) can be written

$$\frac{\partial \mathbf{U}}{\partial t}+\mathrm{div}\mathbf{F}(\mathbf{U})=\mathbf{B}(\mathbf{U}), \tag{21}$$

with

$$\mathbf{U}=\begin{pmatrix} h \\ q_x \\ q_y \end{pmatrix},\quad \mathbf{F}(\mathbf{U})=\begin{pmatrix} q_x & q_y \\ \frac{q_x^2}{h}+\frac{g}{2}h^2 & \frac{q_x q_y}{h} \\ \frac{q_x q_y}{h} & \frac{q_y^2}{h}+\frac{g}{2}h^2 \end{pmatrix}, \tag{22}$$

$$\mathbf{B}(\mathbf{U})=\begin{pmatrix} 0 \\ \gamma_x gh+\frac{1}{\rho}T_x \\ \gamma_y gh+\frac{1}{\rho}T_y \end{pmatrix}, \tag{23}$$

where $\mathbf{q} = h\mathbf{u}$ is the material flux.

[19] The equations are discretized here on general triangular grids with a finite element data structure using a particular control volume which is the median based dual cell (Figure 2a). The finite element grid is appropriate to describe variable topography and refinement is performed when strong topographic gradients occur. Dual cells C_i are obtained by joining the centers of mass of the triangles surrounding each vertex P_i. We use the following notations:

K_i set of nodes P_j surrounding P_i,
A_i area of C_i;
Γ_{ij} boundary edge belonging to cells C_i and C_j;
L_{ij} length of Γ_{ij};
$\mathbf{n}_{ij}$ unit normal to Γ_{ij}, outward to C_i.

If P_i is a node belonging to the boundary Γ of the numerical domain, we join the centers of mass of the triangles adjacent to the boundary to the middle of the edge belonging to Γ (see Figure 2b). Let Δt denote the time step, $\mathbf{U}_i^n$ the approximation of the cell average of the exact solution at time t^n

$$\mathbf{U}_i^n \simeq \frac{1}{A_i}\int_{C_i}\mathbf{U}(t^n,x)dx, \tag{24}$$

and $\mathcal{B}(\mathbf{U}_i^n)$ the approximation of the cell average of the exact source term at time t^n

$$\mathcal{B}(\mathbf{U}_i^n) \simeq \frac{1}{A_i}\int_{C_i}\mathbf{B}(\mathbf{U}_i^n)dx. \tag{25}$$

Then the finite volume scheme writes

$$\mathbf{U}_i^{n+1}=\mathbf{U}_i^n-\sum_{j\in K_i}\alpha_{ij}\mathcal{F}\left(\mathbf{U}_i^n,\mathbf{U}_j^n,\mathbf{n}_{ij}\right)+\Delta t\mathcal{B}\left(\mathbf{U}_i^n\right), \tag{26}$$

with

$$\alpha_{ij}=\frac{\Delta t L_{ij}}{A_i}, \tag{27}$$

and where $\mathcal{F}$ ($\mathbf{U}_i^n$, $\mathbf{U}_j^n$, $\mathbf{n}_{ij}$) denotes an interpolation of the normal component of the flux $\mathbf{F}(\mathbf{U}) \cdot \mathbf{n}_{ij}$ along the edge Γ_{ij}. The treatment of the boundary conditions (i. e. the calculation of the boundary fluxes) using a Riemann invariant is addressed by *Bristeau et al.* [2001].

[20] The main difficulty is to compute fluxes at the control volumes interfaces Γ_{ij} and the overall stability of the method requires some upwinding in the interpolation of the fluxes [*Audusse et al.*, 2000]. The computation of these fluxes constitutes the major difference between the kinetic scheme used here and Godunov-type methods which are very accurate for shock capturing, but not well suited to deal with vacuum front at the margins of the avalanche where the system looses hyperbolicity ($h = 0$ corresponding here to dry soils). This drawback results to the lack of definable wave speeds in advance of a flow front. Many shock capturing upwind schemes produce negative heights at these points and subsequently break down or become unstable. An artificial small height of fluid in the whole domain has to be imposed to stabilize the scheme [e.g., *Mangeney et al.*, 2000]. *Tai* [2000] and *Tai et al.* [2002] overcome this imperfection by tracking the vacuum front. *Denlinger and Iverson* [2001] calculate the theoretical speed of a flow front using the Riemann invariant of the wave emanating from the front directed in the inner part of the mass. We follow here an alternative approach to solve the Saint Venant equations by using a kinetic solver, which is intrinsically able to treat vacuum and is also appropriate to handle

discontinuous solutions. These properties are of highest importance for gravitational flow modeling. One further important property of this scheme is that it does not require any dimensional splitting. To our knowledge, this type of schemes has never been applied to avalanche flow modeling over slopping topography.

3.2. Kinetic Formulation

[21] The kinetic approach consists in using a fictitious description of the microscopic behavior of the system to define numerical fluxes at the interface of an unstructured mesh. Macroscopic discontinuities disappear at the microscopic scale. We will introduce here the main concept of the kinetic scheme used in this model. A complete description of this scheme and its numerical implementation is done by *Audusse et al.* [2000] and *Bristeau et al.* [2001]. The scheme will be discussed by omitting the friction term which is further introduced using a semi-implicit scheme (see section 3.3). In this method, fictitious particles are introduced and the equations are considered at the microscopic scale where no discontinuities occur. A distribution function of fictitious particles $M(t, x, y, \boldsymbol{\xi})$ with velocity $\boldsymbol{\xi}$ is introduced in order to obtain a linear microscopic kinetic equation equivalent to the macroscopic equations (21), (22), and (23). The microscopic density M of particle present at time t in the vicinity $\Delta x\, \Delta y$ of the position (x, y) and with a velocity $\boldsymbol{\xi}$ is defined as

$$M(t,x,y,\boldsymbol{\xi}) = \frac{h(t,x,y)}{c^2}\chi\left(\frac{\boldsymbol{\xi}-\mathbf{u}(t,x,y)}{c}\right), \tag{28}$$

with a "fluid density" h, a "fluid temperature" proportional to

$$c^2 = \frac{gh}{2}, \tag{29}$$

and $\chi(\boldsymbol{\omega})$ a positive, even function defined on $\Re^2$ and satisfying

$$\int_{\Re^2}\chi(\boldsymbol{\omega})d\boldsymbol{\omega} = 1, \int_{\Re^2}\omega_i\omega_j\chi(\boldsymbol{\omega})d\boldsymbol{\omega} = \delta_{ij}, \tag{30}$$

with δ_{ij} the Kronecker symbol and $\boldsymbol{\omega} = (\omega_x, \omega_y)$. This function χ is assumed to be compactly supported, i. e.

$$\exists\, \omega_M \in \Re, \text{such that } \chi(\boldsymbol{\omega}) = 0 \quad \text{for } \| \boldsymbol{\omega} \| \geq \omega_M. \tag{31}$$

where the rectangular function χ given by *Bristeau et al.* [2001] read

$$\chi(\boldsymbol{\omega}) = \begin{cases} \frac{1}{12} & \text{for } |\omega_i| \leq \sqrt{3}, \quad i = x, y. \\ 0 & \text{otherwise} \end{cases} \tag{32}$$

Note that the rectangular shape of the distribution function χ imposed for the fictitious particles would change in time if real particles where considered. Simple calculations show that the macroscopic quantities are linked to the microscopic density function by the relations

$$\mathbf{U} = \int_{\Re^2}\begin{pmatrix}1\\ \boldsymbol{\xi}\end{pmatrix}M(t,x,y,\boldsymbol{\xi})d\boldsymbol{\xi}, \tag{33}$$

$$\mathbf{F}(\mathbf{U}) = \int_{\Re^2}\begin{pmatrix}\boldsymbol{\xi}\\ \boldsymbol{\xi}\otimes\boldsymbol{\xi}\end{pmatrix}M(t,x,y,\boldsymbol{\xi})d\boldsymbol{\xi}, \tag{34}$$

$$\mathbf{B}(\mathbf{U}) = g\gamma\int_{\Re^2}\begin{pmatrix}1\\ f\boldsymbol{\xi}\end{pmatrix}\bigtriangledown_{\boldsymbol{\xi}} M(t,x,y,\boldsymbol{\xi})d\boldsymbol{\xi}, \tag{35}$$

These relations imply that the nonlinear system (18), (19), (20) is equivalent to the linear transport equation for the quantity M, for which it is easier to find a simple numerical scheme with good properties

$$\frac{\partial M}{\partial t} + \boldsymbol{\xi}.\bigtriangledown_{\mathbf{x}} M - g\gamma.\bigtriangledown_{\boldsymbol{\xi}} M = Q(t,x,y,\xi), \tag{36}$$

for some collision term $Q(t, x, y, \xi)$ which satisfies

$$\int_{\Re^2}\begin{pmatrix}1\\ \boldsymbol{\xi}\end{pmatrix}Q(t,x,y,\boldsymbol{\xi})d\boldsymbol{\xi} = 0. \tag{37}$$

As usual, the "collision term" $Q(t, x, y, \xi)$ in this kinetic representation of the Saint Venant equations, which relaxes the kinetic density to the Gibbs equilibrium M, is neglected in the numerical scheme, i. e. in each time step we project the kinetic density on M, which is a way to perform all collisions at once and to recover the Gibbs equilibrium without computing it [e.g., *Perthame and Simeoni*, 2001]. Finally, the discretization of this simple kinetic equation allows to deduce an appropriate discretization of the macroscopic system. A simple upwind scheme is applied to the microscopic equation (36) leading to the formulation of the fluxes defined in equation (26):

$$\mathcal{F}(\mathbf{U}_i, \mathbf{U}_j, \mathbf{n}_{ij}) = \mathbf{F}^+(\mathbf{U}_i, \mathbf{n}_{ij}) + \mathbf{F}^-(\mathbf{U}_j, \mathbf{n}_{ij}), \tag{38}$$

$$\mathbf{F}^+(\mathbf{U}_i, \mathbf{n}_{ij}) = \int_{\boldsymbol{\xi}.\mathbf{n}_{ij}\geq 0}\boldsymbol{\xi}.\mathbf{n}_{ij}\begin{pmatrix}1\\ \boldsymbol{\xi}\end{pmatrix}M_i(\boldsymbol{\xi})d\boldsymbol{\xi}, \tag{39}$$

$$\mathbf{F}^-(\mathbf{U}_j, \mathbf{n}_{ij}) = \int_{\boldsymbol{\xi}.\mathbf{n}_{ij}\leq 0}\boldsymbol{\xi}.\mathbf{n}_{ij}\begin{pmatrix}1\\ \boldsymbol{\xi}\end{pmatrix}M_j(\boldsymbol{\xi})d\boldsymbol{\xi}. \tag{40}$$

The simple form of the density function (here a rectangle-type function Π) allows analytical resolution of integrals (39), (40) and gives the possibility to write directly a finite volume formula, which therefore avoids using the extra variable $\boldsymbol{\xi}$ in the implementation of the code. The resulting numerical scheme is consistent and conservative. Furthermore, it is proved that the water height positivity is preserved under the Courant Friedrichs Levy condition [*Audusse et al.*, 2000]

$$\Delta t \max\left(|u_i^n| + \omega_M c_i^n\right) \leq \frac{A_i}{\sum_{j\in K_i} L_{ij}}. \tag{41}$$

[22] In comparison with flood modeling, avalanche modeling introduces a further difficulty relating to the property of granular media able to remain static (solid) even with an inclined free surface. This equilibrium is not intrinsically preserved by the finite volume scheme and specific

processing has to be introduced in the numerical scheme for the particular case of kinetic scheme, as will be developed in section 3.3.

3.3. Friction

[23] The friction is introduced here by using a projection method on the domain of admissible stresses defined by the Coulomb friction law [see, e.g., *Staron*, 2002]. The implicit treatment of the friction is done by using the discretized set of equation (26)

$$h_i^{n+1} = h_i^n - \sum_{j\in K_i} \alpha_{ij} \mathcal{F}_h\left(\mathbf{U}_i^n, \mathbf{U}_j^n, \mathbf{n}_{ij}\right), \tag{42}$$

$$\mathbf{q}_i^{n+1} = \mathbf{q}_i^n - \sum_{j\in K_i} \alpha_{ij} \mathcal{F}_{\mathbf{q}}\left(\mathbf{U}_i^n, \mathbf{U}_j^n, \mathbf{n}_{ij}\right) + g h_i^{n+1} \boldsymbol{\gamma}_t \Delta t + \frac{1}{\rho} \mathbf{T}_{ti}^{n+1} \Delta t, \tag{43}$$

where $\boldsymbol{\gamma}_t = (\gamma_x, \gamma_y)$, with the complementary inequality

$$\| \mathbf{T}_{ti}^{n+1} \| \geq \mu\rho g \gamma_z h_i^{n+1} \Rightarrow \mathbf{T}_{ti}^{n+1} = -\mu\rho g \gamma_z h_i^{n+1} \frac{\mathbf{u}_i^{n+1}}{\| \mathbf{u}_i^{n+1} \|}, \tag{44}$$

$$\| \mathbf{T}_{ti}^{n+1} \| < \mu\rho g \gamma_z h_i^{n+1} \Rightarrow \mathbf{u}_i^{n+1} = 0, \tag{45}$$

Equation (43) shows the linear variation of the traction as a function of $\mathbf{q}_i^{n+1}$

$$\mathbf{T}_{ti}^{n+1} = \frac{\rho}{\Delta t} \mathbf{q}_i^{n+1} - \frac{\rho}{\Delta_t} \tilde{\mathbf{q}}_i^{n+1}, \tag{46}$$

where

$$\tilde{\mathbf{q}}_i^{n+1} = \mathbf{q}_i^n - \sum_{j\in K_i} \alpha_{ij} \mathcal{F}_{\mathbf{q}}\left(\mathbf{U}_i^n, \mathbf{U}_j^n, \mathbf{n}_{ij}\right) + g h_i^{n+1} \gamma_t \Delta t \tag{47}$$

(i.e., the solution of equation (43) without any friction term). As the Coulomb friction does not change the direction of the velocity, the flux $\mathbf{q}_i^{n+1}$ has the same direction of the trial $\tilde{\mathbf{q}}_i^{n+1}$. Furthermore, $\mathbf{T}_t$ acts in the opposite direction of the velocity. Equation (46) reduces in the direction of the flow to a scalar equation

$$T_{ti}^{n+1} = \frac{\rho}{\Delta t} q_i^{n+1} - \frac{\rho}{\Delta t} \tilde{q}_i^{n+1}, \tag{48}$$

Figure 3 shows the admissible state of the traction T_{ti} defined by equations (44) and (45) and the family of straight lines (equation (48)) with slope ρ/Δ_t defining the relation between the traction and the algebraic value of the flux q_i^{n+1}. Note that $-(\rho/\Delta\, t)\, \tilde{q}_i^{n+1}$ is the value of T_{ti} at $q_i^{n+1} = 0$. It appears from Figure 3 that if the norm of the driving force $(\rho/\Delta t)\tilde{\mathbf{q}}_i^{n+1}$ is lower than the Coulomb threshold $\sigma_c = \mu\rho g \gamma_z h_i^{n+1}$, the admissible traction T_{ti} is also lower than σ_c and the mass stops, i. e.

$$\frac{\| \tilde{\mathbf{q}}_i^{n+1} \|}{\Delta t} < \mu g \gamma_z\, h_i^{n+1} \Rightarrow\ \mathbf{q}_i^{n+1} = 0. \tag{49}$$

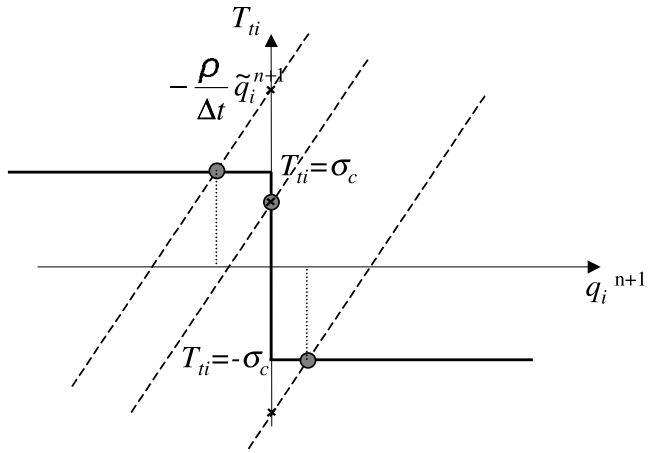

Figure 3. Resolution of the tangential traction by projection on the admissible state imposed by the Coulomb friction law. Solid lines represent the domain of admissible state of the traction, dashed lines represent the family of straight lines obtained from the momentum conservation equation. Circles represent the solution of the problem (three possibilities depending on the relative value of $(\rho/\Delta\, t)$ $\tilde{q}_i^{n+1}$ and σ_c).

On the other hand, if the driving force $(\rho/\Delta t)\tilde{\mathbf{q}}_i^{n+1}$ is higher than the Coulomb threshold then the admissible value of the traction is equal to σ_c and equation (43) read

$$\mathbf{q}_i^{n+1} = \left(\| \tilde{\mathbf{q}}_i^{n+1} \| - \mu g \gamma_z\, h_i^{n+1} \Delta t\right) \frac{\tilde{\mathbf{q}}_i^{n+1}}{\| \tilde{\mathbf{q}}_i^{n+1} \|}. \tag{50}$$

In the case of the flow variable friction law, the friction term is linearized by taking the value of the velocity at time n in the equation (15). Note that, numerically, the resolution process leads to take the positive part on the right hand side of equation (50).

[24] This threshold-type behavior is generally not taken into account in numerical models due to the resulting discontinuity in the velocity field even though it may be useful for avalanches coming to rest and for the starting phase of the avalanche. Generally, the magnitude of the driving force and the Coulomb friction force are compared only for parts of the flow where $\mathbf{u} = 0$ [e.g., *Mangeney et al.*, 2000].

[25] Classical kinetic schemes do not allow the mass stopping when h gradients are nonequal to zero even though its velocity is equal to zero. In fact, for the kinetic scheme based on a rectangle-type distribution function χ (see equation (28)), perturbations propagate at velocity $\tilde{c} = \sqrt{gh}$ even though the fluid is at rest because the "temperature" is non equal to zero. Perturbation linked to the h gradient of a nonflat free surface generates fluxes and the fluid never stops if its free surface is not horizontal. In the opposite, the Coulomb criterion imposes that under a given threshold, a perturbation (e.g., a perturbation of the surface elevation) does not propagate. It can be represented by a fluid at a "temperature" equal to zero, so that the local speed of propagation of disturbance relative to the moving stream is equal to zero. It can be obtained by using a Dirac

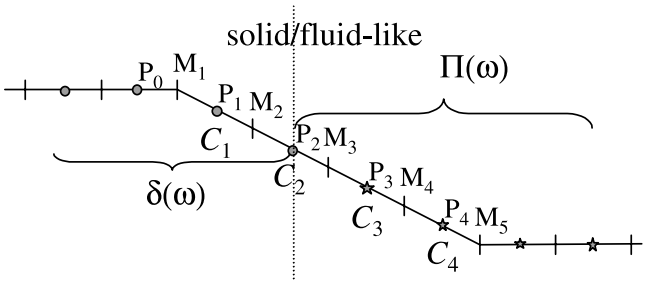

Figure 4. One-dimensional mesh and dual cell C_i with center P_i. Circles denote the points under the Coulomb threshold, and stars denote the points above the Coulomb threshold.

distribution for the function χ. The idea of the present scheme is to introduce a zero temperature fluid with a Dirac-type density of particles M when the fluid is under the Coulomb threshold and a nonzero temperature fluid using a rectangular type density of particles when the fluid is over the Coulomb threshold

$$\| \tilde{\mathbf{q}}_i^{n+1} \| - \mu g \gamma_z h^{n+1} \Delta t < 0 \Rightarrow M(t,x,y,\xi) = h(t,x,y)\delta(\xi - \mathbf{u}(t,x,y)), \quad (51)$$

$$\| \tilde{\mathbf{q}}_i^{n+1} \| - \mu g \gamma_z h^{n+1} \Delta t \geq 0 \Rightarrow M(t,x,y,\xi) = \frac{h(t,x,y)}{c^2} \chi\left(\frac{\xi - \mathbf{u}(t,x,y)}{c}\right), \quad (52)$$

where χ is the rectangular function Π (equation (32). The expression of the flux related to the edge Γ_{ij} in the mass conservation equation using equation (39) read then

$$\| \tilde{\mathbf{q}}_i^{n+1} \| - \mu g \gamma_z h^{n+1} \Delta t < 0 \Rightarrow \mathbf{F}_h^+(\mathbf{U}_i, \mathbf{n}_{ij}) = h_i u_{i,n} Y(u_{i,n}), \quad (53)$$

$$\| \tilde{\mathbf{q}}_i^{n+1} \| - \mu g \gamma_z h^{n+1} \Delta t \geq 0, \Rightarrow \mathbf{F}_h^+(\mathbf{U}_i, \mathbf{n}_{ij}) = \frac{1}{2} h_i u_{i,n} + \frac{\sqrt{3}}{4} h_i c_i + \frac{1}{4\sqrt{3}} h_i \frac{u_{i,n}^2}{c_i}, \quad (54)$$

where Y is the Heaviside distribution and $u_{i,n}$ is the velocity in the normal direction of the edge Γ_{ij}. Similar expression is obtained for $\mathbf{F}^-(\mathbf{U}_j, \mathbf{n}_{ij})$. In the situation of equation (53) (i.e., under the Coulomb threshold), implicit resolution is performed by using the velocity $u_{i,n}$ at time $n + 1$ so that $u_{i,n} = 0$ and $\mathbf{F}_h^+(\mathbf{U}_i, \mathbf{n}_{ij}) = \mathbf{F}_h^-(\mathbf{U}_i, \mathbf{n}_{ij}) = 0$. Note that the Dirac distribution does not allow to recover the momentum equation. In fact the flux calculated for the momentum equation using this function reads

$$\mathbf{F}_q^+(\mathbf{U}_i, \mathbf{n}_{ij}) = h_i u_{i,n}^2 Y(u_{i,n}) \quad (55)$$

without the pressure gradient due to the zero temperature fluid. However, when the fluid is under the Coulomb threshold, the momentum equation is replaced by

$$\mathbf{q} = 0, \quad (56)$$

so that the Dirac-type function is only used in the calculation of the fluxes in the mass conservation equation.

[26] The first step of the numerical scheme is to evaluate the grid points that are under the Coulomb threshold using $\tilde{\mathbf{q}}_i^{n+1}$. Let us look at the simple one-dimensional (1-D) case (Figure 4) where the points P_0, P_1, and P_2 are under the Coulomb threshold (solid circles) and the points P_3 and P_4 are above this threshold (stars). In order to obtain the flux $F_{h,i} = F_h^+(P_{i-1}) + F_h^-(P_i)$ at the interface M_i allowing to satisfy conservation laws, the same distribution function has to be used in both side of the interface: a rectangular distribution is imposed if one of the two points P_i or P_{i-1} is above the Coulomb threshold and a Dirac distribution elsewhere. As a result, the flux through the interface M_3 is calculated using a rectangular function whereas the flux through the interface M_2 is calculated using the Dirac function. The solid/fluid-like transition is then exactly at the point P_2. At this point, the propagation of the h gradient is allowed to the right where the fluid is above the Coulomb threshold and forbidden to the left where the fluid is under the Coulomb threshold. Numerical test show that this method is mass conservative.

[27] The resulting 2-D scheme consists in evaluating at time t the points under the Coulomb threshold, and at time $t + dt$ in calculating the flux F_h through an interface M_{ij} of a cell C_i (1) using the rectangular distribution if one of the two points P_i, P_j situated on both sides of this interface is above the Coulomb threshold, and (2) using a Dirac distribution if the two points P_i, P_j are under the Coulomb threshold. The numerical method can be illustrated on the 2-D mesh presented in Figure 5 where the points M_1, M_2, M_3, P_2, M_{10}, M_{11} surrounding the point P_1 are under the Coulomb threshold. The fluxes F_h through the interfaces of the cell C_1 is then calculated using the Dirac distribution whereas in the cell C_4, all the fluxes are calculated using the rectangular distribution. For the cell C_2, the surrounding points P_3 and M_8 being above the Coulomb threshold, the fluxes F_h through the edges cutting P_2M_8, P_2P_3 are calculated using the rectangular distribution while the fluxes F_h through the edges cutting P_2P_1, P_2M_3, P_2M_9, P_2M_{10} are

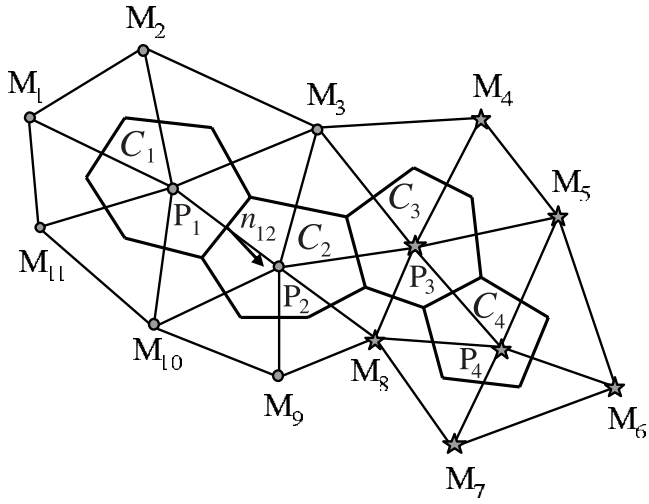

Figure 5. Triangular mesh and dual cell C_1, C_2, C_3, C_4. Circles denote the points under the Coulomb threshold, and stars denote the points above the Coulomb threshold.

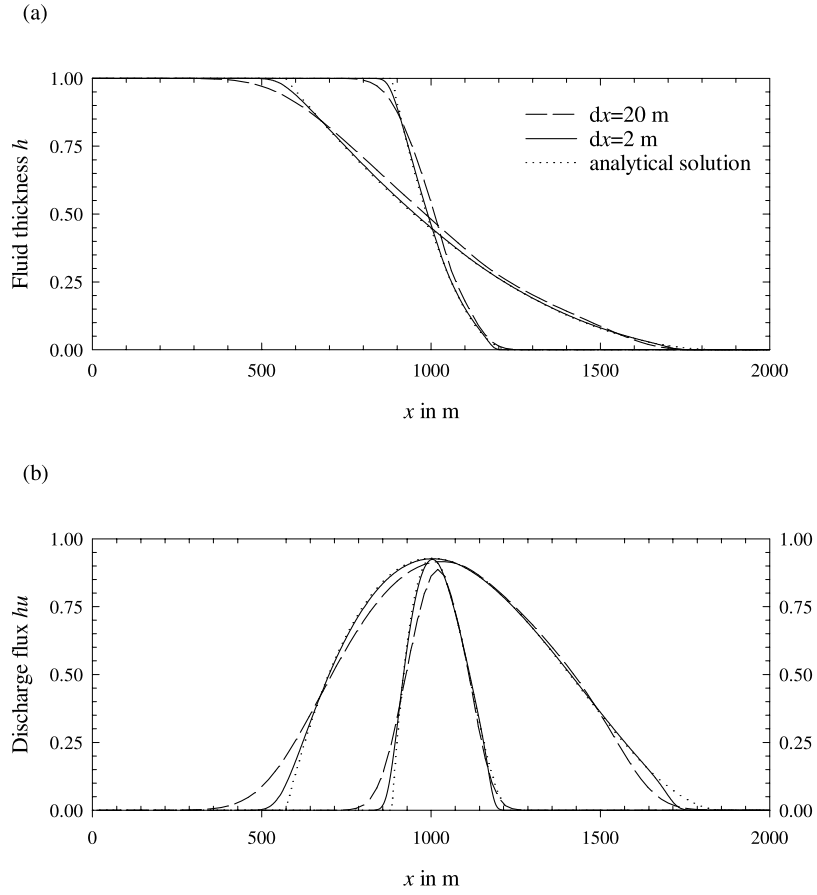

Figure 6. (a) Fluid height h and (b) discharge flux hu versus distance obtained for $\delta = 0°$ and $\theta = 0°$, at times $t = 37$ s and $t = 137$ s calculated with the analytical solution (dotted lines) and with the numerical model for $dx = 20$ m (dashed lines) and $dx = 2$ m (solid lines).

calculated using the Dirac distribution. With this scheme preserving mass conservation at the machine accuracy, the fluid is able to stop.

4. Validation

[28] The precision and performance of the numerical model is tested by comparing numerical results with those of an analytical solution which takes into account a Coulomb-type friction at the base of the flow, provided the angle of friction is smaller than the slope angle and the fluid never stops on the inclined plane [*Mangeney et al.*, 2000]. The test case consists of the instantaneous release of a fluid mass of 1 m high on a dry flat bottom, infinitely long in the negative x direction. The numerical domain ranges from 0 m to 2000 m. Note that the aspect ratio of the geometry considered here is $\epsilon = 10^{-3}$, so that the long-wave approximation is valid. All 1-D numerical experiments are carried out with the 2-D model using the same number of points in the transversal direction (101 points with the same space step as in the flow direction).

[29] From Figures 6 and 7, showing the comparison between analytical and numerical solution for two grid steps ($dx = 20$ m and $dx = 2$ m), it can be observed that the numerical model provides a good representation of the dam break problem as well without and with a friction law. The main difference between analytical and numerical results is located at the front position and at the corner of the dam as was observed by *Mangeney et al.* [2000] with a Godounov-type numerical model. Note that the deviation from the analytical solution is qualitatively the same with the Godounov-type model and the kinetic model: the corner at the left discontinuity is rounded and the position of the front is lower than the position of the analytical front after a few seconds: the shock is smoothed as usual with a first-order scheme as was observed by *Audusse et al.* [2000].

[30] Finally, the results are expressed in terms of the mean relative error dh

$$dh = \frac{\Sigma (h - h_a)^2}{\Sigma h_a^2}, \tag{57}$$

where h_a is the analytical solution for h, and Σ represents the sum over a fixed interval including the points where $0 < h < h_0$. Figure 8 shows that when the space step is reduced by a factor 10, the mean relative error is reduced by a factor about 4 which is compatible with other general convergence rates that can be proved for simple models in the presence of singularities [e.g., *Perthame*, 2002]. Similar results are obtained when the error on hu is considered.

5. Simulation of Experimental Results

[31] Simulation of the experimental results of *Pouliquen* [1999] have been performed in order to evaluate the ability

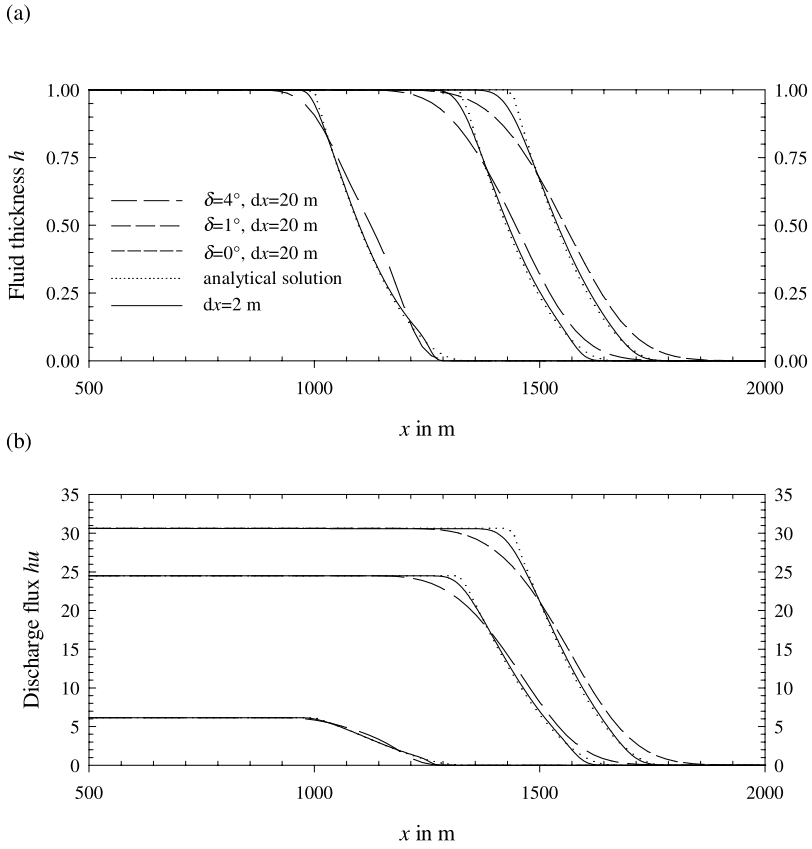

Figure 7. (a) Fluid thickness h and (b) discharge flux hu versus distance obtained for $\delta = 0°$, $\delta = 1°$, and $\delta = 4°$ for inclination angle $\theta = 5°$, at time $t = 35$ s calculated with the analytical solution (dotted lines) and with the numerical model for $dx = 20$ m and $dx = 2$ m (solid lines).

of the model to reach correct steady state, to be able to deal with shocks and to reproduce the arrest phase. In these experiments, glass beads are released from a reservoir through a gate and flow down an inclined plane. These simulations have been performed by imposing solid wall conditions (i.e., $\mathbf{u} \cdot \mathbf{n}_y = 0$, where n_y is the unit outward normal to the y boundary) at the y boundaries of a rectangular domain 2 m long in the x direction and 70 m wide in the y direction. The experimental setup consists of granular material of diameter 0.5 mm ± 0.04 over a rough bed obtained by gluing one layer of particles with the same diameter on the inclined surface. For angles ranging between $\delta_1 = 20.7$ and $\delta_2 = 32.8$ (see equation (15)) this unsteady situation evolves toward a steady state. The friction law (15) has been deduced from these steady flows leading to the fitting parameter $d = 0.98$ mm. The implementation of this flow law in the numerical model allows to reproduce exactly the observed steady states reached by the unsteady initial flow (Figure 9a). Furthermore, simulation exactly reproduces the arrest phase obtained by suddenly

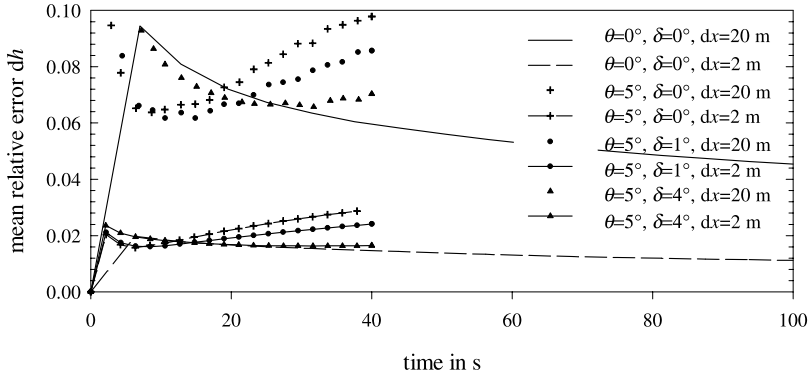

Figure 8. Mean relative error Δh for the dam break problem for $dx = 20$ m (symbols) and $dx = 2$ m (solid lines with symbols) for inclination angle of the bottom $\theta = 5°$ with various angle of friction $\delta = 0°$, $\delta = 1°$ and $\delta = 4°$ and mean relative error Δh for $\theta = 0°$ ($dx = 20$ m solid lines; $dx = 2$ m dashed lines).

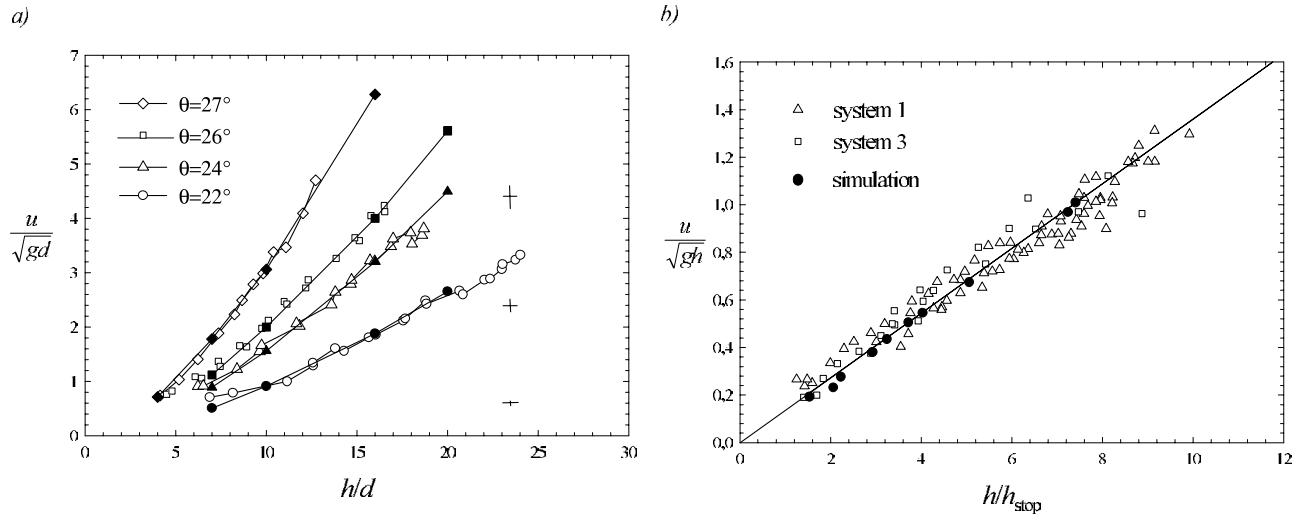

Figure 9. (a) Dimensionless velocity $u/\sqrt{gd}$ as a function of h/d for different inclination angles. (b) Froude number $u/\sqrt{gh}$ as a function of $h/h_{stop}(\theta)$ for different inclinations (experimental results of *Pouliquen* [1999] in open symbols and numerical results in solid symbols).

closing the gate of the reservoir once a thick flow has developed. The shock introduced by suddenly setting the height equal to zero at the left x boundary of the domain is well handled by the numerical model. Figure 9b shows that the final deposit h_{stop} left on the plane is exactly simulated by the model. Note that the flow law (15) has been obtained for values of the Froude number $Fr > \beta$. The simulation of the arrest phase requires the interpolation of the empirical flow law (15) for low Froude number ($Fr < \beta$) to verify $h = h_{stop}$ for $u = 0$.

6. Simulation Over Simplified Topography

[32] To illustrate the capability of the numerical model, a series of numerical experiments have been performed using the above described friction laws over simplified transversally uniform 2-D geometry. These simulations are only for demonstration purposes. If the schematic character of the numerical experiment do not allows to determine the best rheology explaining the flow of natural avalanches, it highlights some specific properties of each friction law and provides a way to analyze the details of the forces within the avalanche.

[33] As an example, let us consider an exponential shape for the topography $z = b(x)$ with characteristic dimensions of the order of real topographies (e.g., the White River valley in Montserrat island (Lesser Antilles)) and uniform in the y direction. Let us investigate the influence of the various flow law in the range of parameters allowing the mass to stop around the position $x = 4500$ m corresponding approximately to some observed runout distances in volcanic areas (e.g., the Boxing Day debris avalanche in Montserrat). The altitude of this topography decreases from roughly 900 m at the top with a maximum slope inclination of 35° to 0 m with slope inclination of a few degrees (almost horizontal in the right part) at $x = 4500$ m (Figure 10a). The corresponding angle is defined by

$$\theta(x) = \theta_0 \exp\left(-\frac{x}{a}\right), \tag{58}$$

with $\theta_0 = 35°$ and $a = 1750$ m (Figure 10b). The results are presented in the coordinate system (x, z) linked to the topography. The initial conditions are defined by the instantaneous release of a parabolic mass over a rigid topography represented in Figure 10a in the coordinate system (x, z)

$$h(x, t = 0) = K\left(l - (x - x_0)^2\right), \tag{59}$$

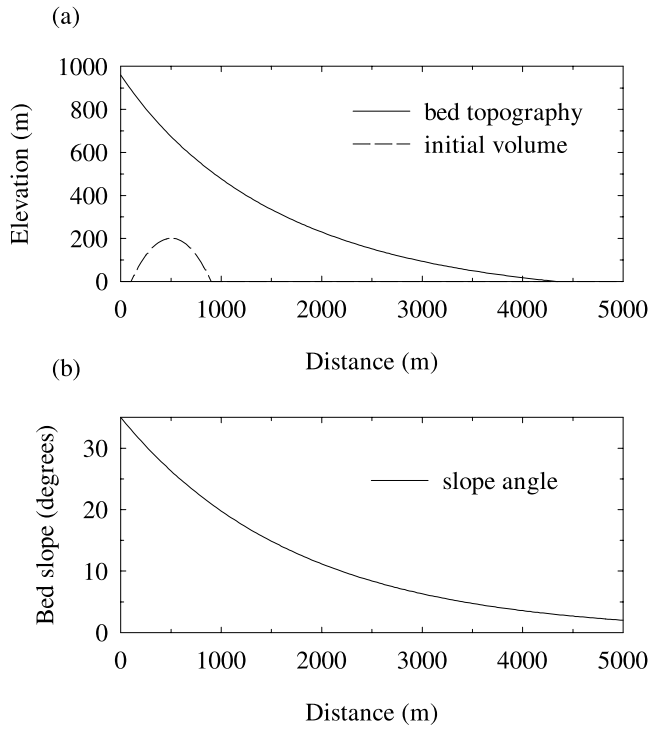

Figure 10. (a) Bed topography in the Cartesian coordinates $(\tilde{x}, \tilde{z})$ and initial volume of the granular mass in the topography-linked coordinates (x, z) and (b) slope angle $\theta(x)$ of the bed in degrees in the topography-linked coordinates (x, z).

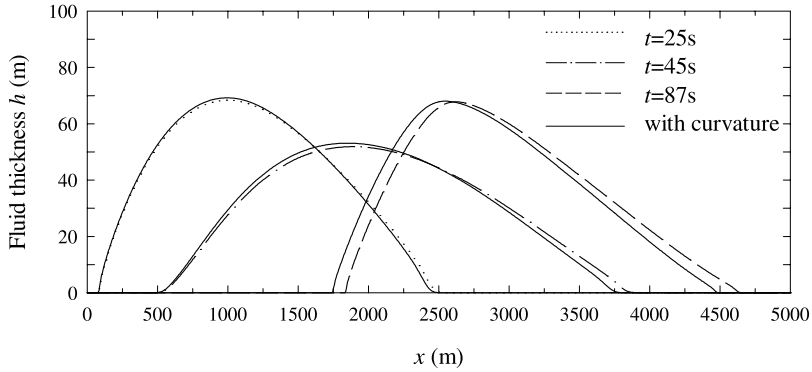

Figure 11. Fluid thickness h at t = 25 s, t = 45 s, and t = 87 s (i.e., when the fluid stops) with and without the curvature term for a simple friction law with $\delta = 15°$. The dash-dotted lines represent the result without curvature effect, and the corresponding solid lines represent those with curvature effect at the same time. Note that the fluid stops at approximatively the same time.

$$u(x, t = 0) = 0, \tag{60}$$

with $K = 1.26 \times 10^{-3}$ m^{-1}, $l = 1.6 \times 10^{5}$ m^2 and $x_0 = 500$ m. Initially, the maximal thickness of the mass is 200 m in the direction perpendicular to the topography with a length of 800 m close to the estimations of the Boxing Day debris avalanche destabilized mass [*Sparks and Young*, 2002]. The numerical domain is discretized using 880 points in the x direction with a space step of 6.25 m and 220 points in the y direction with the same space step. Solid wall boundary conditions ($\mathbf{u}.\mathbf{n}_y = 0$) are imposed in the left and right y limits of the numerical domain.

6.1. Curvature Effects

[34] Note that the equations (19) and (20) are obtained by neglecting the first-order curvature terms. At first order for transversally uniform topography in the y direction, curvature effects lead to an additional friction force linked to centrifugal acceleration. According to the scale analysis of *Gray et al.* [1999] this first-order curvature effect is taken into account by a term involving the curvature radius of the bed profile R in the momentum equation

$$\frac{\partial}{\partial t}(hu) + \frac{\partial}{\partial x}\left(hu^2\right) + \frac{\partial}{\partial y}(huv) = \gamma_x gh + \frac{\partial}{\partial x}\left(g\gamma_z \frac{h^2}{2}\right) - \mu h\left(g\gamma_z + \frac{u^2}{R}\right)\frac{u_x}{\| \mathbf{u} \|}. \tag{61}$$

$$\frac{\partial}{\partial t}(hv) + \frac{\partial}{\partial x}(huv) + \frac{\partial}{\partial y}\left(hv^2\right) = \gamma_y gh + \frac{\partial}{\partial y}\left(g\gamma_z \frac{h^2}{2}\right) - \mu h\left(g\gamma_z + \frac{u^2}{R}\right)\frac{u_y}{\| \mathbf{u} \|}. \tag{62}$$

When either μ or $\lambda = L/R_c$, where R_c is a characteristic value of the curvature radius, or both are smaller than $O(\epsilon^{\frac{1}{2}})$ and when u does not become too large, then this term may be dropped in comparison with the others terms [*Greve and Hutter*, 1993].

[35] Numerical tests show that the first-order curvature effects involved in the last term of equations (61) and (62) is not too large in our case, where the radius of curvature is relatively high. Note that in the present case, ϵ is of order 0.1, $\mu = 0.27$ for $\delta = 15°$ is of order $\epsilon^{\frac{1}{2}}$ and λ is lower than 4×10^{-3}. Figure 11 shows that the results with and without this curvature term are close to each other for a simple friction law with $\delta = 15°$, especially during the flow. Furthermore, the fluid stops almost at the same time (t = 86.4 s without curvature effects and t = 86 s with curvature effects) and the maximum elevation of the deposit is the same ($h_{\max}$ = 67.8 m without curvature and $h_{\max}$ = 68 m with curvature). However, a difference of 156 m (5% of the deposit length) is observed in the runout distance. These curvature effects may be important in most real situations (R. P. Denlinger, personal communication, 2003). When the curvature effects are not taken into account, i.e., when the exponential shape does not slow down the granular mass, the front is located further away. The empirical nature of the friction angle in such a model is well illustrated in this example. In fact, curvature effects are difficult to take into account in two dimensions when the geometry is not transversally uniform due to the existence of various curvature radii. Dropping these effects leads to unverifiable error in the determination of the well fitted friction angle because the tuned parameter obtained for fitting a runout distance may be dependent on these local effects. In the following simulations, the first-order curvature effects have been taken into account.

6.2. Coulomb Friction Law

[36] Let us first look at the results obtained by using the friction law with a constant angle δ. Sensitivity study is performed just by varying the value of this angle. The avalanche deposit extends further for lower values of δ as shown in Figure 12 where the geometry of the deposits is obtained when the flow comes to rest. A difference of approximatively 740 m on the front position is obtained when δ varies from 14° to 16° and a difference of approximatively 1060 m when δ varies from 16° to 20°. Furthermore, the length of the deposit is larger and the maximum elevation lower when the friction angle decreases. The deposit extends along 2900 m when δ = 14° with a maximum elevation h = 65 m while the extension is only 2290 m when δ = 20° with a maximum elevation h = 75 m. It appears that only low values of the friction angle around 15° are appropriate to reproduce the

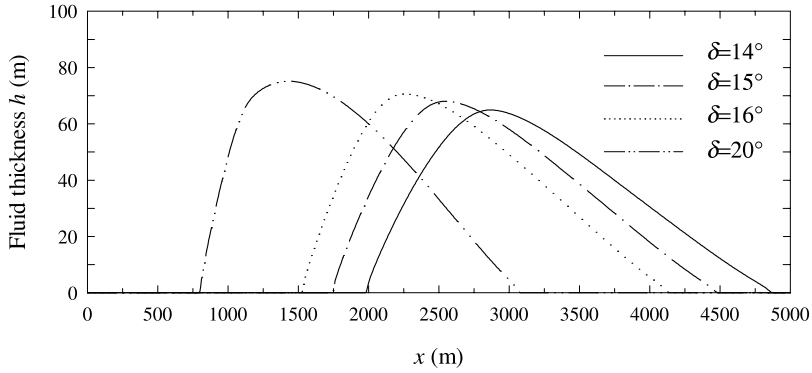

Figure 12. Profile of the mass at the time when the fluid stops for various values of the friction angle δ using the simple friction law.

great mobility of real debris avalanche as was generally observed in the simulations of real avalanches. The low value of δ is a consequence of the widely observed ability of large avalanches to travel distances much larger than expected from classical models of slope failure. Note that in spite of the extreme simplification of this test the calculated values are in the range of the deposit's elevation estimated from geological observation [*Sparks and Young*, 2002]. The *x* position of the maximum elevation is situated toward the rear of the mass. In fact, with a constant friction angle, in the accelerating stage, the fluid flows with higher velocity near the front than near the rear due to a driving negative *h* gradient. The positive *h* gradient near the downhill rear of the fluid plays a braking role in the balance of forces by slowing the flow as the frictional force f_x do (Figure 13). It is worth pointing out that the force due to the pressure gradient (i. e. the *h* gradient) is relatively small compared with the other forces as well at $t = 25$ s as at $t = 65$ s in the rest of the mass. This feature may explain the weak effect of the earth pressure coefficients involved in the pressure gradient when nonisotropy of normal stresses is assumed [see, e.g., *Pouliquen and Forterre*, 2002].

[37] For this configuration of initial mass and such a topography, the inertial forces are important during the flow contrary to those obtained in the simulation over low angle

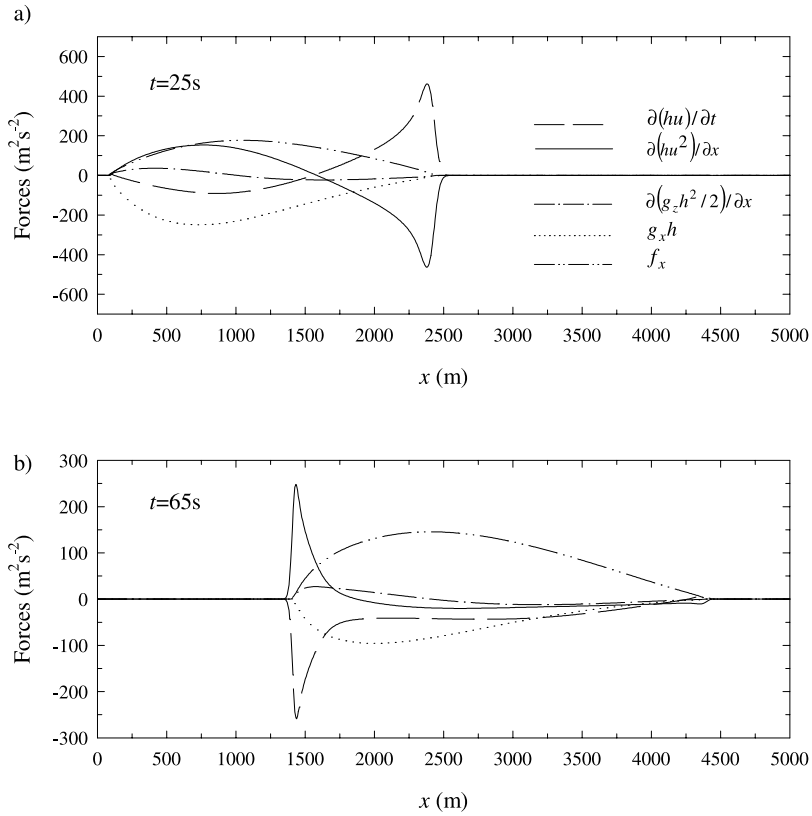

Figure 13. Forces involved in the *x* momentum equation for a simple friction law with $\delta = 15°$ versus distance (a) at time $t = 25$ s and (b) at $t = 65$ s, f_x represents the frictional force.

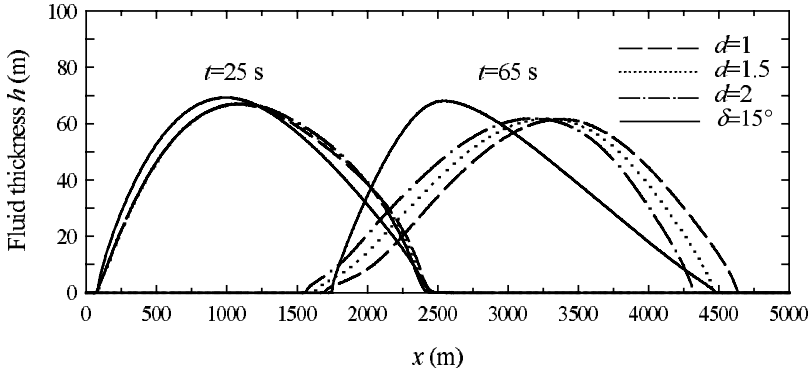

Figure 14. Fluid thickness at t = 25 s, and when the fluid stops for various values of d in the Pouliquen's flow law with $\delta_1 = 13°$ and $\delta_2 = 20°$ and for a simple friction law with $\delta = 15°$. The dash-dotted lines represent the result for the Pouliquen's flow law and the corresponding solid lines represent those for the simple friction law.

inclined plane close to the experimental setup presented in section 5. In our case the influence of the vertical profile choosen for the horizontal velocity should not be negligible.

6.3. Pouliquen's Friction Law

[38] We propose to use here the recent law developed empirically by *Pouliquen* [1999] (see section 2.2). Contrary to the one parameter simple friction law, three parameters have to be determined: two friction angles δ_1 and δ_2 and the coefficient d. Debris avalanches are composed of particles with sizes varying from less than a millimeter to tens of meters. It is therefore difficult to estimate the value of d in the model. However a value of d = 1.5 m allows the mass reaching x = 4500 m for the tuned values $\delta_1 = 13°$ and $\delta_2 = 20°$ (Figure 14). Note that the well-fitted angle $\delta = 15°$ obtained with the constant angle friction law range between these tuned values. Only such low values of δ_1 and δ_2 (compared to the angles obtained experimentally) allow to reproduce the expected runout distance. The variation of δ with the position is represented in Figure 15 at the instants t = 25 s and t = 65 s for d = 1, d = 1.5 and d = 2. The friction angle evolves in time as a function of the flow parameters (h, hu) (Figure 15). Note that for low value of d the results are similar to those obtained for simple friction law with $\delta = 13°$ and for high values of d the results are close to those obtained using a simple friction law with $\delta = 20°$. In this range of values, the flow is governed by δ_2 near the front and rear of the flow and by δ_1 in the inner part of the mass. Difference of more than 1 degree is observed on δ when d value goes from 1 to 2 leading to strong difference in the deposit (Figure 14). Figure 14 shows that the shapes of the flowing mass at t = 25 s are similar both for various values of d and for the simple friction law. During the flowing stage, the friction force does not play the leading role as it is illustrated in Figure 16a at t = 25 s. During the deceleration stage, the importance of the friction force increases (Figure 16b) to the stopping stage where the friction force balanced by the gravity force dominates the other forces. Concerning the deposit, not only the runout distance changes with d but the shape too. As d increases the front becomes more marked and the rear finer. Such a shape seems to be closer to real observed front of avalanches. The shape of the deposit using Pouliquen's friction law with d = 1.5 is quite different from this obtained by simple friction law with $\delta = 15°$ even though the runout distance is the same and the extension of the deposit is similar (see Figure 14). The downhill part of the deposit using this variable friction angle is 18 m high 250 m from the rear and 35 m high for constant friction angle. Contrary to simple friction law, the maximum thickness is situated near the front for Pouliquen's flow law due to low friction for high elevation in the inner part of the avalanche. As was

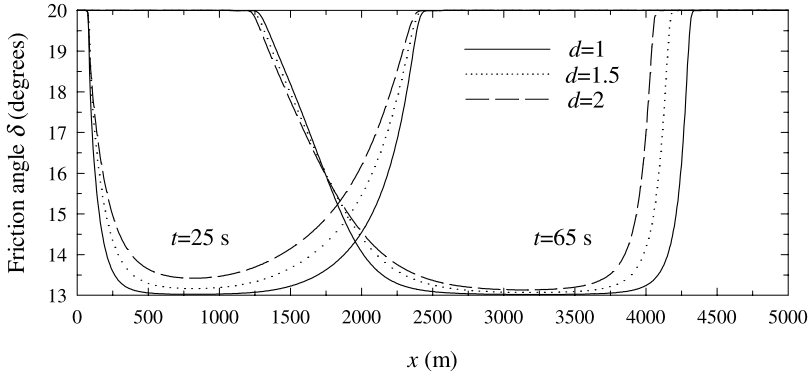

Figure 15. Friction angle δ versus position x in Pouliquen's flow law with $\delta_1 = 13°$ and $\delta_2 = 20°$ and d = 1 (solid lines), d = 1.5 (dotted lines) and d = 2 (dashed lines) at times t = 25 s and t = 65 s. At the rear and the front, i.e., for small values of h, the friction angle tends to δ_2.

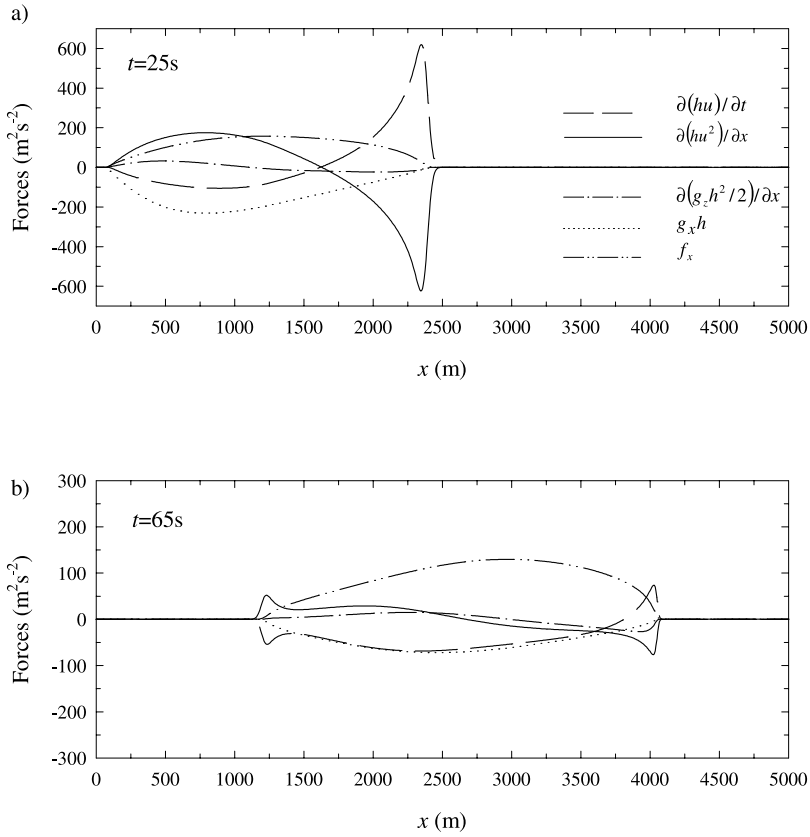

Figure 16. Forces involved in the x momentum equation for Pouliquen's flow law with $\delta_1 = 13°$ and $\delta_2 = 20°$ and $d = 1.5$ versus distance at times (a) $t = 25$ s and (b) $t = 65$ s; f_x represents the frictional force.

observed for simple friction law, the force due to the pressure gradient is relatively small compared with the other forces as well at $t = 25$ s as at $t = 65$ s except at the front (Figure 16).

6.4. Mass Stopping

[39] The major originality of this model is the explicit introduction of the stopping in the kinetic scheme. Let us look with more details at this stopping stage illustrated in Figures 17 and 18 for simple friction law and Pouliquen's flow law, respectively. For simple friction law ($\delta = 15°$), the mass stops at $t = 86$ s and for Pouliquen's flow law ($\delta_1 = 13°$, $\delta_2 = 20°$, $d = 1.5$) at $t = 97.6$ s. With these rheological parameters, the runout distance for both simple friction law and Pouliquen's flow law is approximatively 4500 m. With the constant angle friction law, the front, encountering low slope begins to stop. The stopping propagates toward the rear of the mass until the whole fluid stops. The asymmetric shape becomes more pronounced when the fluid stops due to this downward propagation of the stopping stage.

[40] Note that with this topography and with this initial released mass, the Coulomb threshold is never reached in the rear of the flow for friction angle higher than $\delta = 23°$. For such high friction, the front stops and this stopping propagates toward the rear. However, the driving force and in particular the gravity near the rear of the flow is still higher than the Coulomb threshold due to high slope of the topography. In this case, the h gradient may play a significant role by controlling the balance of forces. As an example, at $t = 70$ s for $\delta = 24°$, the whole fluid is stopping except a 150 m long part in the rear of the mass. What is really meant is that this uphill part of the avalanche, under the Coulomb threshold, behaves like a fluid in the sense that is relaxes to equilibrium with horizontal free surface suggesting the existence of horizontal surfaces in the deposit. This is possible because it is stopped by a solid-like part farther downslope. The presence of a fluid-like zone behind a rigid mass would be an interesting point to verify by comparing numerical results derived from mathematical models with empirical or geological observation of deposits. The stopping scenario is not the same for Pouliquen's flow law where the central part of the fluid is stopping first (Figure 18). In this case, the friction angle is not constant as was observed in the preceding section. The difference in the stopping behavior of a mass controlled by simple friction law or Pouliquen's flow law can be a useful test to determine the more appropriate flow law.

[41] The presence of a fluid-like zone behind a solid-like mass is also observed for example with rheological parameters $\delta_1 = 12°$, $\delta_2 = 20°$ and $d = 10$. Further analysis of this phenomenon require the development of a model reproducing the equilibrium of a fluid at rest [see, e.g., *Perthame and Simeoni*, 2001]. Such a new model preserving the equilibrium of a lake at rest has been proposed by *Bouchut et al.* [2003].

7. Conclusion

[42] Numerical modeling of debris avalanche has been presented here based on Savage and Hutter's equations.

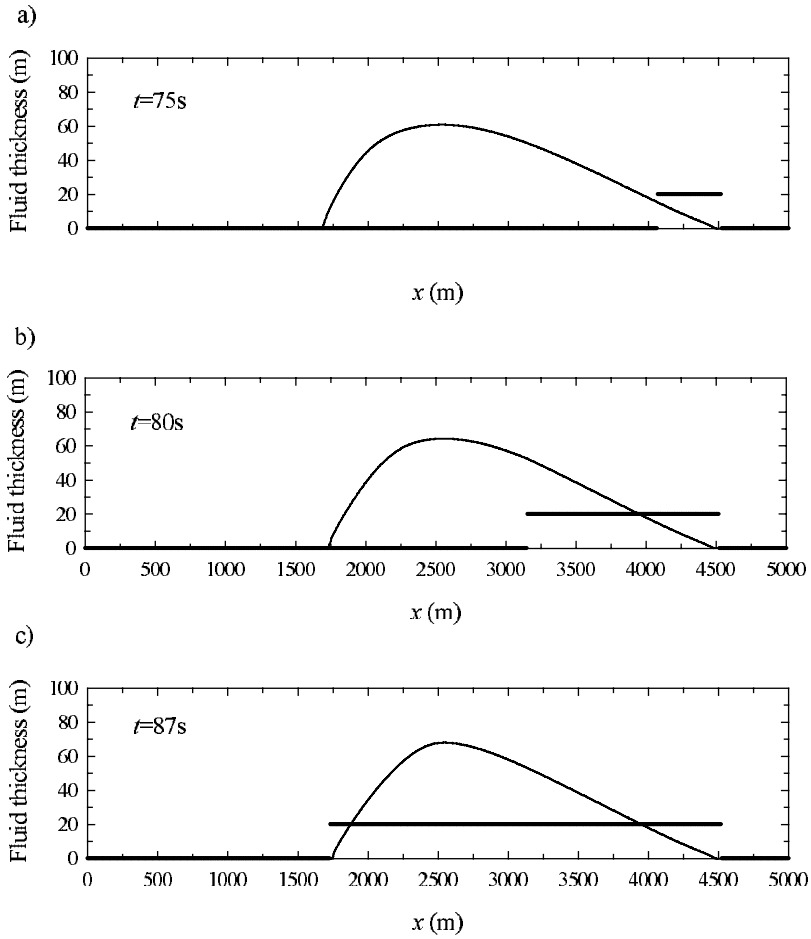

Figure 17. Fluid thickness (solid lines) versus distance at (a) $t = 75$ s, (b) $t = 80$ s, and (c) $t = 87$ s during the stopping stage for simple friction law with $\delta = 15°$. A value of 0 is allocated to the fluid under the Coulomb threshold, and a value of 20 is allocated to the fluid above the Coulomb threshold.

Granular avalanche behavior has been described using a Coulomb-type friction law with constant and flow variable friction angle.

[43] The numerical model is based on a kinetic scheme. The main idea was to introduce two different descriptions of the microscopic behavior of the system suggested by the ambivalence of the solid/fluid-like behavior of granular material. The resulting solver appears to be stable and preserves height positivity, contrary to several Godounov-type methods. Efficiency of this model has been tested by comparing with analytical solution of dam break problem and with experimental results. The numerical scheme remains stable in spite of the introduction of the discontinuous Coulomb criterium. Furthermore, the discretization on a finite element mesh is well suited to simulate avalanches over real complex topographies.

[44] Preliminary simulations on a simplified geometry have allowed us to test the capability of the numerical model and to compare constant and variable angle friction laws. The shape of the deposit strongly depends on the used friction law. Pouliquen's flow law with a friction angle depending on the height and velocity leads to steepest front of the granular deposit with more elongating rear. Furthermore, the stopping stage differs depending on the flow law. While the stopping propagates from the front to the rear when a constant friction angle is used, the inner part of the mass begins to stop when Pouliquen's flow law is used. This feature may be a useful tool to determine the best fitted flow law when comparing with experimental results.

[45] Numerical modeling of debris avalanche provides the only way to estimate typical velocities and relative weight of the involved forces. The above analysis shows that the h gradient force does not play a significant role in the studied example except at the rear and front of the granular mass. The friction force begins to be a leading force only when the granular mass approaches the stopping stage. A better understanding of avalanche flow and stopping dynamics and the evaluation of the appropriate flow law will improve prediction of the stopping location, flow velocity and impact pressures.

[46] The numerical tests show the possible existence of a fluid-like zone in the deposit under particular conditions. In such situations, part of the fluid remains over the Coulomb threshold subjected for example to high gravity forces. It is still blocked by the down slope deposit and relaxes to equilibrium like a fluid suggesting the existence of horizontal surfaces in the deposit. Observation of such features in real or experimental deposits would be interesting and

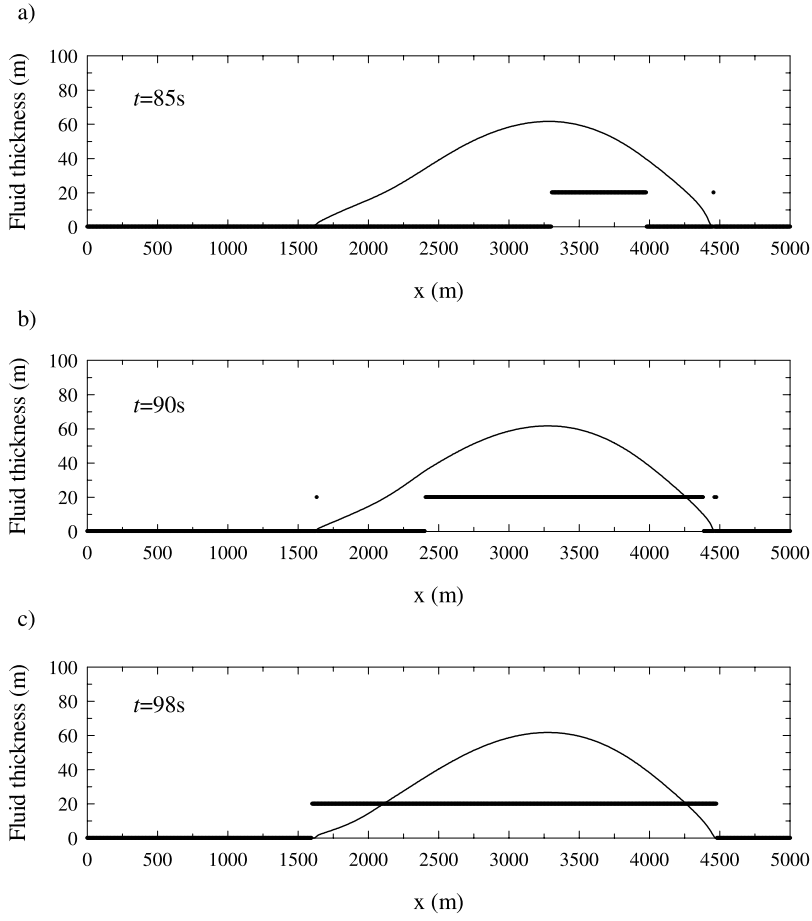

Figure 18. Fluid thickness (solid lines) versus distance at (a) $t = 85$ s, (b) $t = 90$ s, and (c) $t = 98$ s during the stopping stage for Pouliquen's flow law with $\delta_1 = 13°$ and $\delta_2 = 20°$ and $d = 1.5$. A value of 0 is allocated to the fluid under the Coulomb threshold, and a value of 20 is allocated to the fluid above the Coulomb threshold.

may provide information on the mechanical behavior of a granular mass.

[47] **Acknowledgments.** This work was supported by the Action Concertée Incitative (CNRS) and the Action Thématique Incitative Prioritaire (CNRS). We are grateful to O. Pouliquen for fruitful discussions and to R. P. Denlinger for their very interesting review of the paper. Contribution IPGP 1917.

References

Aranson, I. S., and L. S. Tsimring, Continuum description of avalanches in granular media, *Phys. Rev. E.*, 64, 020301(R), 2001.

Arattano, M., and W. Z. Savage, Modelling debris flows as kinematic waves, *Bull. Int. Assoc. Eng. Geol.*, *49*, 3–13, 1994.

Assier-Rzadkiewicz, S., P. Heinrich, P. C. Sabatier, B. Savoye, and J. F. Bourillet, Numerical modelling of a landslide-generated tsunami: The 1979 Nice event, *Pure Appl. Geophys.*, *157*, 1707–1727, 2000.

Audusse, E., M. O. Bristeau, and B. Perthame, Kinetic schemes for Saint-Venant equations with source terms on unstructured grids, *INRIA Rep. 3989*, Natl. Inst. for Res. in Comput. Sci. and Control, Le Chesnay, France, 2000.

Azanza, E., Ecoulements granulaires bidimensionnels sur un plan incliné, Ph.D., thesis, Ecole Natl. des Ponts et Chaussées, Champs sur Marne, France, 1998.

Botchorishvili, R., B. Perthame, and A. Vasseur, Equilibrium Schemes for Scalar Conservation Laws with Stiff Sources, *INRIA Rep. RR-8931*, Natl. Inst. for Res. in Comput. Sci. and Control, Le Chesnay, France, 2000.

Bouchut, F., A. Mangeney-Castelnau, B. Perthame, and J. P. Vilotte, A new model of Saint Venant and Savage-Hutter type for gravity driven shallow water flows, *C.R. Acad. Sci., Ser. I*, *336*, in press, 2003.

Bristeau, M. O., B. Coussin, and B. Perthame, Boundary conditions for the shallow water equations solved by kinetic schemes, *INRIA Rep. 4282*, Natl. Inst. for Res. in Comput. Sci. and Control, Le Chesnay, France, 2001.

Denlinger, R. P., and R. M. Iverson, Flow of variably fluidized granular masses across three-dimensional terrain: 2. Numerical predictions and experimental tests, *J. Geophys. Res.*, *106*(B1), 553–566, 2001.

Douady, S., B. Andreotti, and A. Daerr, On granular surface flow equations, *Eur. Phys. J. B*, *11*, 131–142, 1999.

Gray, J. M. N. T., M. Wieland, and K. Hutter, Gravity driven free surface flow of granular avalanches over complex basal topography, *Proc. R. Soc. London, Ser. A*, *455*, 1841–1874, 1999.

Greve, R., and K. Hutter, Motion of a granular avalanche in a convex and concave chute: Experiments and theoretical predictions, *Proc. R. Soc. London, Ser. A*, *342*, 573–600, 1993.

Greve, R., T. Koch, and K. Hutter, Unconfined flow of granular avalanches along a partly curved surface. I. Theory, *Proc. R. Soc. London, Ser. A*, *445*, 399–413, 1994.

Heinrich, P., G. Boudon, J. C. Komorowvski, R. S. J. Sparks, R. Herd, and B. Voight, Numerical simulation of the December 1997 debris avalanche in Montserrat, Lesser Antilles, *Geophys. Res. Lett.*, *28*, 2529–2532, 2001.

Hunt, B., Asymptotic solution for dam-break problem, *J. Hydraul. Eng.*, *110*(8), 1985.

Hunt, B., Newtonian fluid mechanics treatment of debris flows and avalanches, *J. Hydraul. Eng.*, *120*, 1350–1363, 1994.

Hutter, K., T. Koch, C. Pluss, and S. B. Savage, The dynamics of avalanches of granular materials from initiation to runout. part II., Experiments, *Acta Mech.*, *109*, 127–165, 1995.

Iverson, R. M., The physics of debris flows, *Rev. Geophys.*, *35*(3), 245–296, 1997.

Iverson, R. M., and R. P. Denlinger, Flow of variably fluidized granular masses across three-dimensional terrain: 1. Coulomb mixture theory, *J. Geophys. Res.*, *106*(B1), 537–552, 2001.

Jenkins, J. T., and E. Askari, Hydraulic theory for a debris flow supported on a collisional shear layer, *Chaos*, *9*, 654–658, 1999.

Laigle, D., and P. Coussot, Numerical modeling of mudflows, *J. Hydraul. Eng.*, *123*(7), 617–623, 1997.

Macedonio, G., and M. T. Pareschi, Numerical simulation of some lahars from Mount St. Helens, *J. Volcanol. Geotherm. Res.*, *54*, 65–80, 1992.

Mangeney, A., P. Heinrich, and R. Roche, Analytical Solution for Testing Debris Avalanche Numerical Models, *Pure Appl. Geophys.*, *157*, 1081–1096, 2000.

Naaim, M., and I. Gurer, Two-phase numerical model of powder avalanche theory and application, *Nat. Hazards*, *117*, 129–145, 1998.

Naaim, M., S. Vial, and R. Couture, Saint-Venant approach for rock avalanches modelling, paper presented at Saint Venant Symposium, Univ. Paris, Paris, 28–29 Aug. 1997.

Perthame, B., *Kinetic Formulation of Conservation Laws*, Oxford Univ. Press, New York, 2002.

Perthame, B., and C. Simeoni, A kinetic scheme for the Saint-Venant system with a source term, *Calcolo*, *38*(4), 201–231, 2001.

Pouliquen, O., Scaling laws in granular flows down rough inclined planes, *Phys. Fluids*, *11*(3), 542–548, 1999.

Pouliquen, O., and Y. Forterre, Friction law for dense granular flows: Application to the motion of a mass down a rough inclined plane, *J. Fluid Mech.*, *453*, 133–151, 2002.

Sabot, F., M. Naaim, F. Granada, E. Surinach, P. Planet, and G. Furdada, Study of avalanche dynamics by seismic methods, image-processing techniques and numerical models, *Ann. Glaciol.*, *26*, 319–323, 1998.

Savage, S. B., and K. Hutter, The motion of a finite mass of granular material down a rough incline, *J. Fluid Mech.*, *199*, 177–215, 1989.

Savage, S. B., and K. Hutter, The dynamics of avalanches of granular materials from initiation to runout. part I: Analysis, *Acta Mech.*, *86*, 201–223, 1991.

Sparks, R. S. J., and S. R. Young, The eruption of Soufrire Hills Volcano, Montserrat: Overview of scientific results, in *The Eruption of Soufrire Hills Volcano, Montserrat, From 1995 to 1999*, edited by T. H. Druitt and B. P. Kokelaar, *Geol. Soc. London Mem.*, 21, 45–69, 2002.

Staron, L., Etude Numérique des Mécanismes de Destabilisation des Pentes Granulaires, Ph.D., thesis, Inst. de Phys. du Globe de Paris, Paris, 2002.

Tai, Y. C., Dynamics of granular avalanches and their simulations with shock-capturing and front-tracking numerical schemes, Ph.D., thesis, Tech. Univ., Darmstadt, Germany, 2000.

Tai, Y. C., S. Noelle, J. M. N. T. Gray, and K. Hutter, Shock-capturing and front-tracking methods for granular avalanches, *J. Comput. Phys.*, *175*, 269–301, 2002.

Toro, E. F., *Riemann Solvers and Numerical Methods for Fluid Dynamics*, 492 pp., Springer-Verlag, New York, 1997.

Whipple, K. X., Open-channel flow of Bingham fluids: Applications in debris-flow research, *J. Geol.*, *105*, 243–262, 1997.

Wieland, M., J. M. N. T. Gray, and K. Hutter, Channelized free surface flow of cohesionless granular avalanches in a chute with shallow lateral curvature, *J. Fluid Mech.*, *392*, 73–100, 1999.

Zwinger, T., Dynamik einer Trockenscheelawine auf beliebig geformten Berghängen, Ph.D., thesis, Tech. Univ. Wien, Vienna, 2000.

F. Bouchut, B. Perthame, and C. Simeoni, Département de Mathématique et Applications, Ecole Normale Supérieure et CNRS, 45 rue d'Ulm, F75230 Paris cedex 05, France. (benoit.perthame@ens.fr; chiara.simeoni@ens.fr)

M. O. Bristeau, Institut National de Recherche en Informatique et en Automatique, Projet M3N, BP 105, F-78153 Le Chesnay Cedex, France. (marie-odile.bristeau@inria.fr)

A. Mangeney-Castelnau and J.-P. Vilotte, Département de Modélisation Physique et Numérique, IPGP, F-75252 Paris cedex 05, France. (mangeney@ipgp.jussieu.fr; vilotte@ipgp.jussieu.fr)

S. Yerneni, Center for Development of Advanced Computing, Pune University Campus, Ganesh Khind, Pune 411 007, India. (sudhakar@cdac.ernet.in)